Supplementary Information

Van der Waals antiferromagnetic proximity effect at $FePS_3$/Pt uncompensated interface

Yinchang Ma[1#], Shijie Xu[1#], Zhuo Chen[1], Chen Liu[1], Tao Yang[1], Yuan Yan[2], Jefferson Zhe Liu[2], Fei Xue[3,4], Xixiang Zhang[1]*

[1]Physical Science and Engineering Division, King Abdullah University of Science and Technology, Thuwal 23955, Saudi Arabia

[2]Department of Mechanical Engineering, The University of Melbourne, Parkville, VIC, 3010, Australia

[3]Center for Quantum Matter, School of Physics, Zhejiang University, Hangzhou 311215, China

[4]ZJU-Hangzhou Global Scientific and Technological Innovation Center, Zhejiang University, Hangzhou, 311215, China

*Email: xixiang.zhang@kaust.edu.sa

[#] Contributed equally

List of contents:

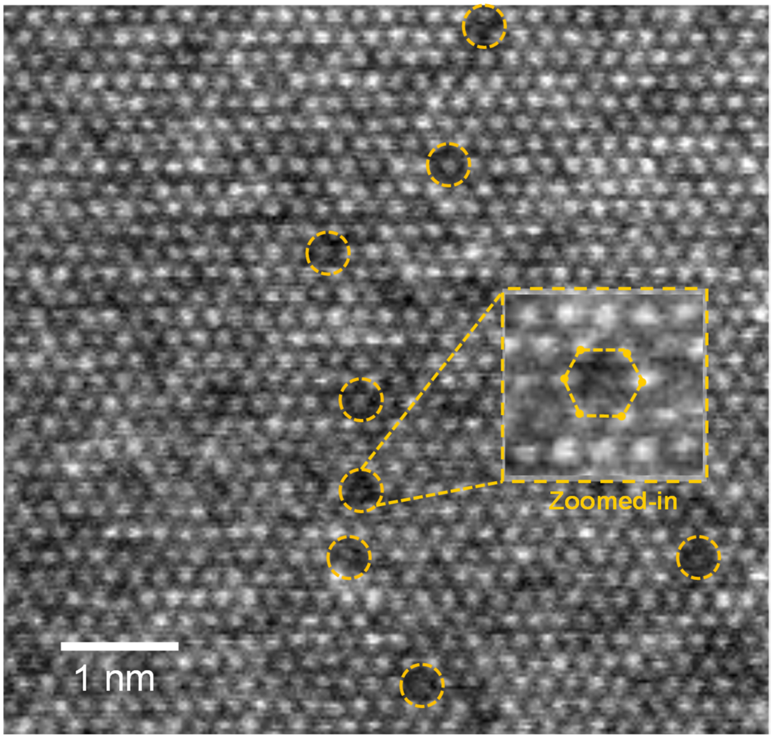

Figure S1. High-resolution transmission electron microscopy image of ultra-thin $FePS_3$ viewed from [001] showing Fe vacancies on the surface. Yellow dashed circles with a zoomed-in inset highlight specific vacancy sites in the lattice.

Table S1. Peak fitting results for Fe 2p XPS spectra

Peak	Area %	FWHM	Max Height	Center (eV)	Fe^{2+} to Fe^{3+} ratio
Fe^{2+} $2p_{3/2}$	24.711	2.5098	2041.7741	710.2318	5.489
Fe^{3+} $2p_{3/2}$	4.5301	1.7573	534.5905	711.9424	
Satellite	31.626	7.0626	928.6428	715.4293	
Fe^{2+} $2p_{3/2}$	17.544	2.8748	1265.5453	723.6843	4.873
Fe^{3+} $2p_{3/2}$	3.624	3.5198	213.5180	726.3806	
Satellite	17.963	5.6094	664.1388	731.0499	

Table S2. Peak fitting results for Fe 3p XPS spectra

Peak	Area %	FWHM	Max Height	Center (eV)	Fe^{2+} to Fe^{3+} ratio
Fe^{2+} $2p_{3/2}$	75.289	2.7579	622.7195	54.7266	3.048
Fe^{3+} $2p_{3/2}$	24.710	3.2222	174.9275	57.9421	

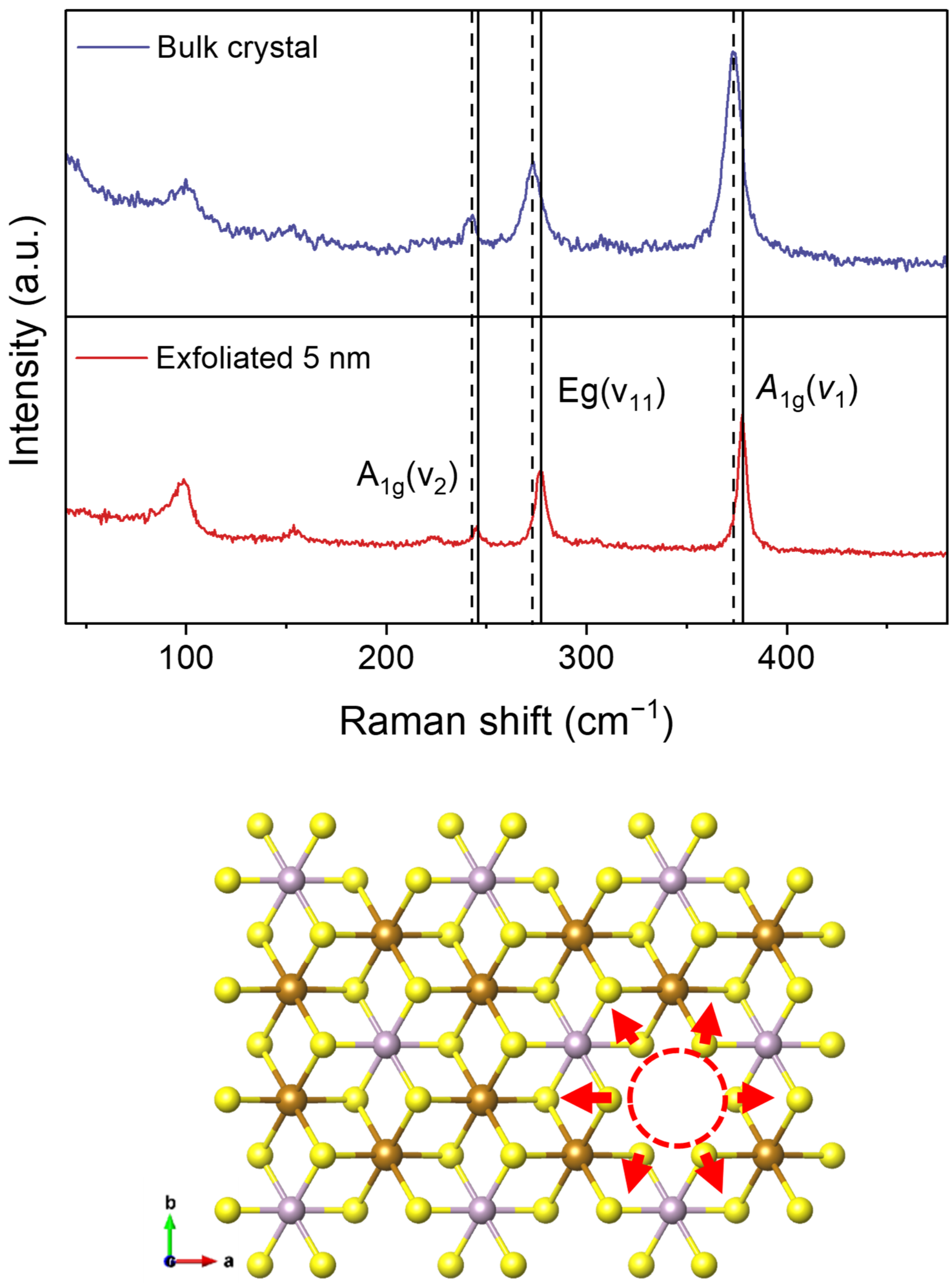

Figure S2. Top panel: Raman spectra of the bulk and exfoliated (20 nm) $FePS_3$ samples. Bottom panel: Strain and bond stiffening around a vacancy resulting in Raman blue shift.

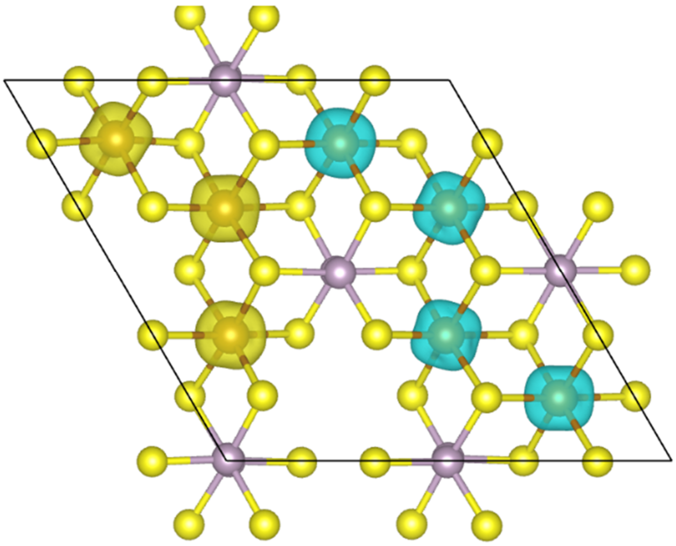

Figure S3. Spin charge density in defective $FePS_3$ viewed from [001]. The yellow and cyan bubbles represent net spin-up and spin-down charge densities, respectively.

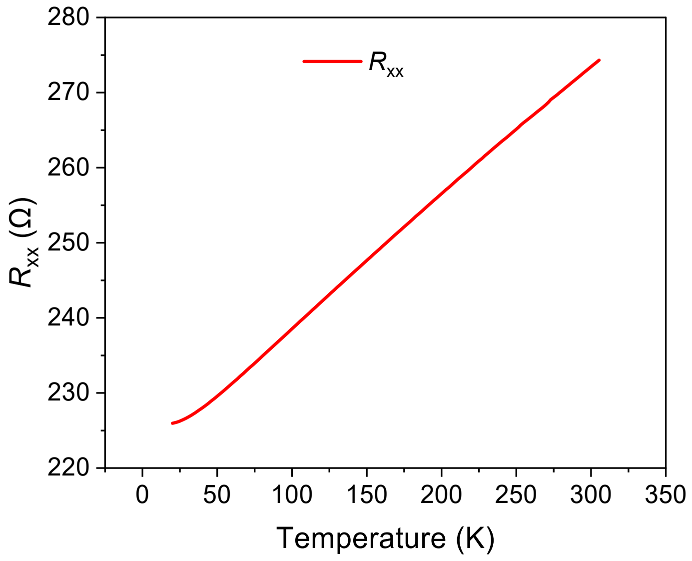

Figure S4. Temperature dependence of R_{xx} showing metallic conductivity.

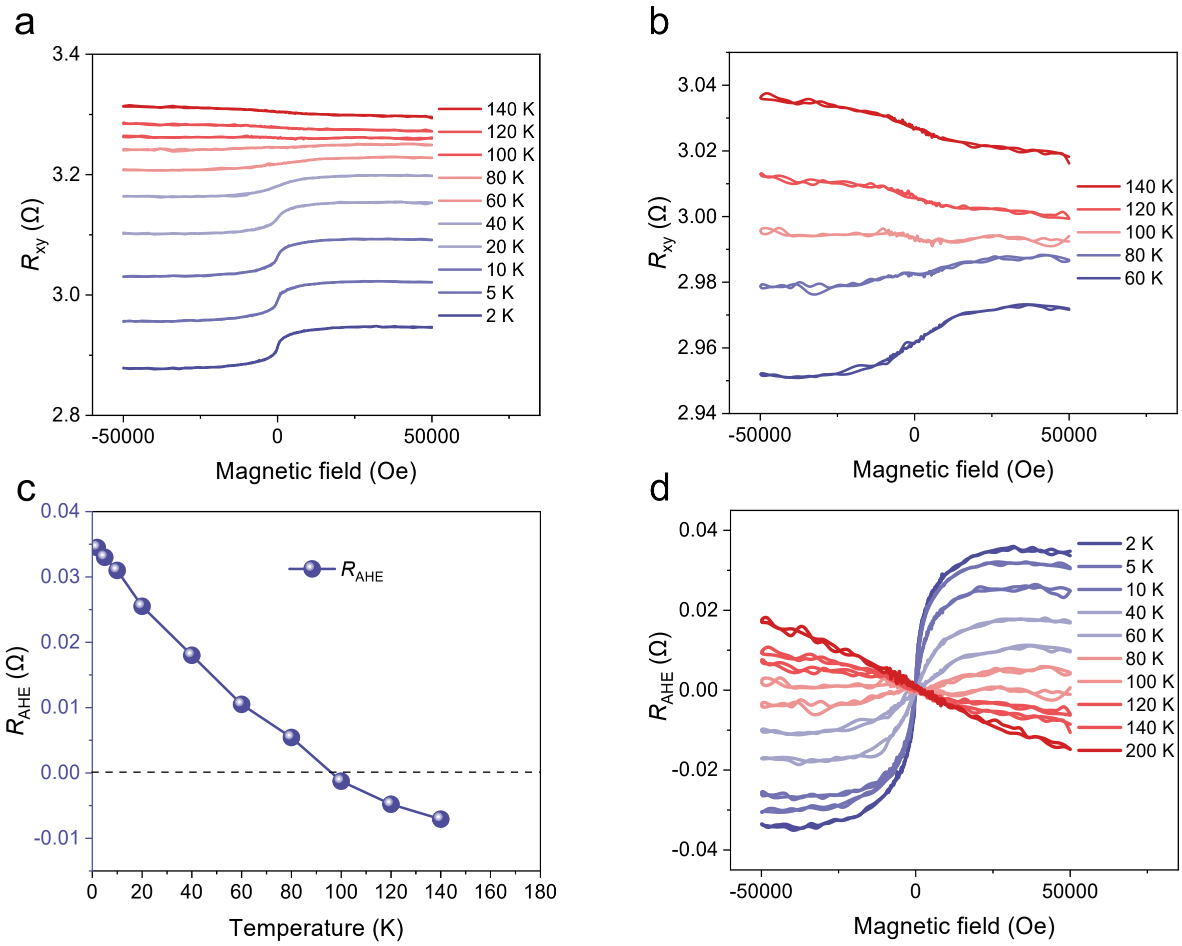

Figure S5. Temperature and magnetic field dependence of transport properties of $FePS_3$/Pt heterostructures with reduced $FePS_3$ thickness (8 nm). (**a**) R_{xy}–H at various temperatures with the fields applied OOP. (**b**) R_{xy} as a function of magnetic field showing the reversal of the sign of the Hall resistance near 100 K. (**c**) Variations of the AHE resistance with temperature. (**d**) R_{AHE}–H plot from 2 to 200 K.

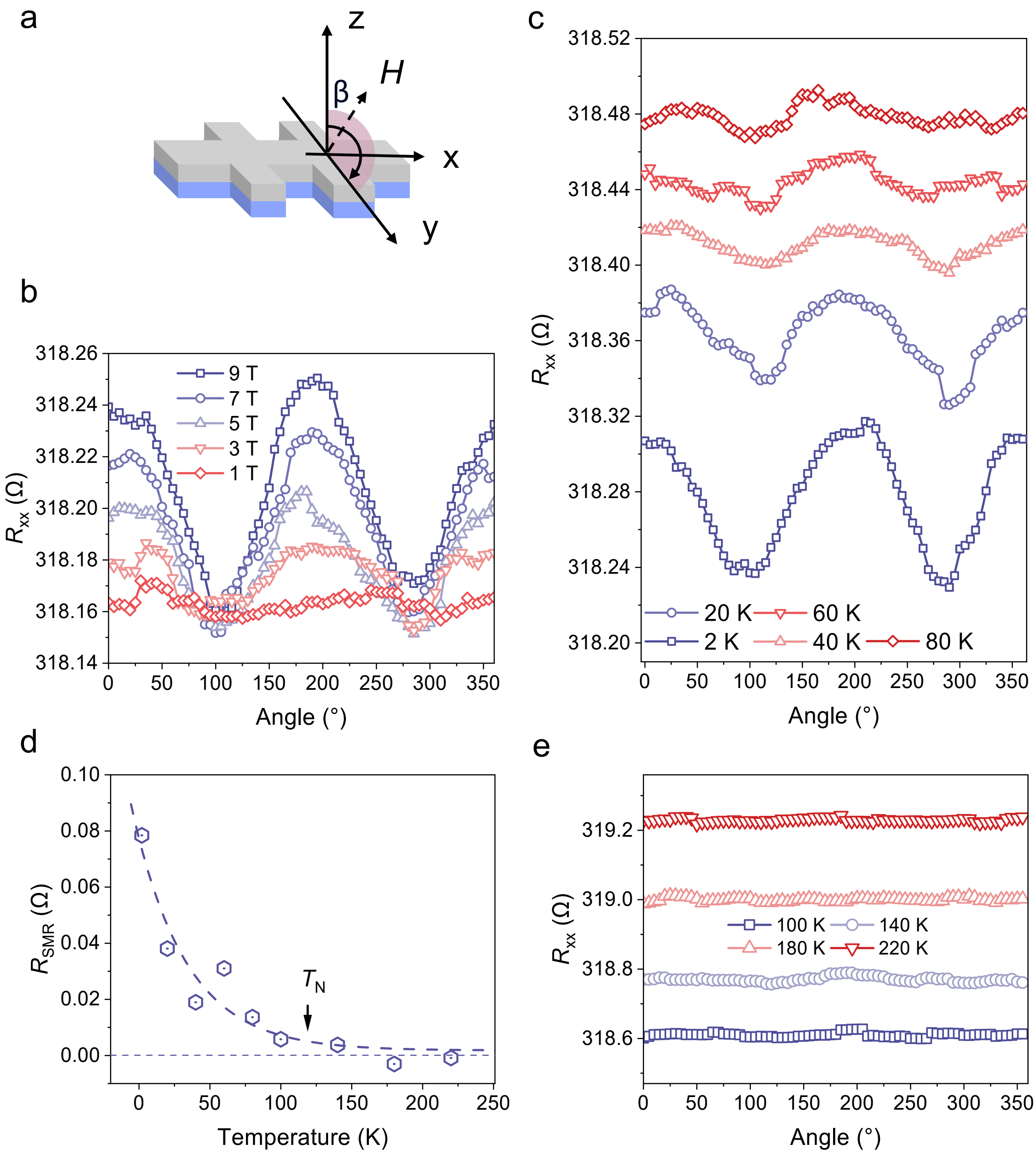

Figure S6. Angular dependence of R_{xx} in $FePS_3$/Pt heterostructure with field rotating in the *y*-*z* plane for SMR measurement. (**a**) Schematic illustration of the measurement setup showing the rotation of the applied magnetic field in the *y*-*z* plane and the angle (*β*) between the field and the *z*-axis. (**b**) R_{xx} as a function of the magnetic field angle at different magnetic field strengths (1 T, 3 T, 5 T, 7 T, and 9 T) at a fixed temperature of 2 K. (**c**) R_{xx} as a function of the magnetic field angle at different temperatures (2 K, 10 K, 40 K, 60 K, and 80 K) at a fixed magnetic field strength of 7 T. (d) Temperature dependence of R_{SMR} extracted from (c) and (e). (e) Angular-dependent R_{xx} at temperatures above 100 K.

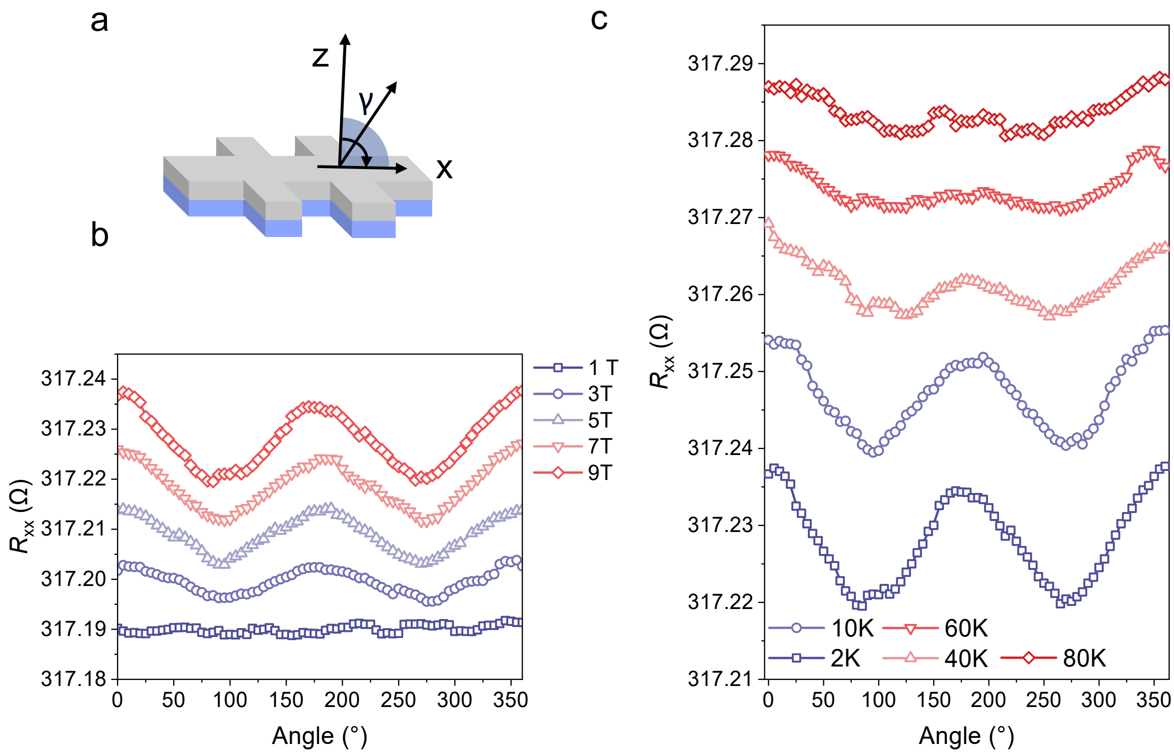

Figure S7. Angular dependence of R_{xx} in $FePS_3$/Pt heterostructures with field rotating in the *x*-*z* plane for AMR measurement. (**a**) Schematic illustration of the measurement setup showing the rotation of the applied magnetic field in the *x*-*z* plane and the angle (γ) between the field and the *z*-axis. The *x*-axis represents the current flow direction, and the *z*-axis represents the OOP direction. (**b**) R_{xx} as a function of the magnetic field angle at different magnetic field strengths (1 T, 3 T, 5 T, 7 T, and 9 T) at a fixed temperature of 2 K. (**c**) R_{xx} as a function of the magnetic field angle at different temperatures (2 K, 10 K, 40 K, 60 K, and 80 K) at a fixed magnetic field strength of 7 T.

	Field (T)	1	3	5	7	9
y-z rotation	R_1 (Ω)	318.164	318.172	318.182	318.191	318.205
	R_{SMR} (Ω)	0.0090	0.0240	0.0530	0.0760	0.0910
	SMR ratio	0.00283%	0.00754%	0.0167%	0.0239%	0.0286%
x-z rotation	R_2 (Ω)	317.190	317.199	317.209	317.218	317.227
	R_{AMR} (Ω)	0.002	0.006	0.0110	0.012	0.014
	AMR ratio	0.000631%	0.00189%	0.00347%	0.00378%	0.00441%

Table S3. Calculated SMR and AMR for the angular dependence of R_{xx} displayed in Figure S6b and S7b using Equations 1 and 2, where the field rotates in the *y*-*z* plane and the *x*-*z* plane, respectively.

Supplementary Note

Through DFT calculations, we can identify the numerical relation between vacancy concentration and magnetization. Figure S8 shows the differential spin charge density distribution for $FePS_3$ with different densities (1/32 and 1/8). It indicates that all Fe spins remain compensated except for the one closest to the vacancy site.

Based on the monolayer vacancy model, we propose the following mathematical expressions to describe the approximate relationship between Fe vacancy concentration (C_v) and magnetization (M):

$$M(C_v) = M_0 + N\alpha C_v \qquad \text{Eq. S1}$$

Where $M\,(C_v)$ is the total net magnetization, M_0 is the net magnetization without Fe vacancies, N is the number of Fe atoms in the layer, α is the magnetization per unit vacancy, and C_v is the Fe vacancy density. From DFT calculations, we estimate that $\alpha \approx 3\mu_B$. For the $FePS_3$ sheets with two different vacancy densities shown in Figure S8, our proposed equation yields magnetization values below:

$$M\left(\frac{1}{32}\right) = 128 \times 3 \times \frac{1}{32} = 12\mu_B;\ M\left(\frac{1}{8}\right) = 32 \times 3 \times \frac{1}{8} = 12\mu_B$$

These values closely match the DFT-calculated magnetization values of $13.3\mu_B$ and $12.5\mu_B$ for corresponding models shown in Figure S8, thus supporting the validity of the proposed equation.

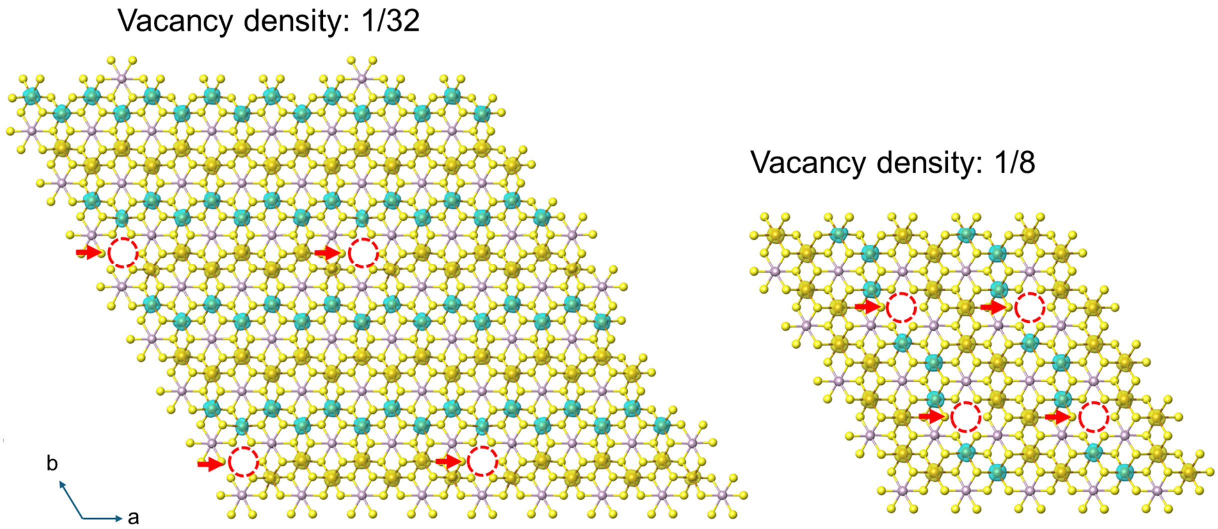

Figure S8. Spin charge density distribution of $FePS_3$ with different Fe vacancy concentrations viewed from c-axis. Red dashed circles and arrows indicate Fe vacancy sites. The yellow and cyan bubbles represent net spin-up and spin-down charge densities, respectively.